Topological modes bound to dislocations in mechanical metamaterials

Jayson Paulose, Bryan Gin-ge Chen, and Vincenzo Vitelli

Instituut-Lorentz, Universiteit Leiden, 2300 RA Leiden, The Netherlands

S1. CALCULATION OF THE TOPOLOGICAL POLARIZATION

Here we summmarize the calculation of the topological polarization following Ref. 1. The topological polarization is calculated from the rigidity, or compatibility, matrix R that relates bond extensions $e_i = R_{ij}u_j$ to site displacements u_i [2, 3]. The first step is to calculate the Fourier-transformed rigidity matrix $R(\mathbf{k})$ whose determinant is complex: $\det R(\mathbf{k}) \equiv |\det R(\mathbf{k})|e^{i\phi(\mathbf{k})}$ (done with a choice of unit cell consistent with the calculations in Ref. 1). Next, the winding numbers, $n_i = \{n_1, n_2\}$, of $\phi(\mathbf{k})$ are evaluated using

$$n_i = -\frac{1}{2\pi}\oint_{C_i} d\mathbf{k} \cdot \nabla_{\mathbf{k}}\phi(\mathbf{k}) \qquad (S1)$$

along the two cycles $\{C_1, C_2\}$ of the Brillouin zone parallel to the reciprocal lattice directions $(\mathbf{b}_1, \mathbf{b}_2)$, defined by $\mathbf{a}_i \cdot \mathbf{b}_j = 2\pi\delta_{ij}$ [1]. The winding numbers are invariants of the gapped lattice; smooth deformations of the triangle shape do not change n_i unless the sites in the lattice lie in a special position and cause the phonon gap to close. We define the topological polarization to be

$$\mathbf{P}_T = \sum_i n_i \mathbf{a}_i. \qquad (S2)$$

This definition of $\mathbf{P}_T$ differs from that of Ref. 1 by a factor of V_{cell} (theirs is strictly speaking a polarization *density*). Our $\mathbf{P}_T$ is equal to $\mathbf{R}_T$ in Ref. 1 since the correction $\mathbf{r}_0 = d\sum_{i \text{ sites}} \mathbf{p}_i - \sum_{j \text{ bonds}} \mathbf{p}_j$ (where $\mathbf{p}_a$ is the position of site / bond a) is equal to zero for our choices of unit cells. For the deformed square lattice used in the main text, the Fourier-transformed rigidity matrix is calculated from the unit cell site positions (given in section S2 B) and bond assignments, and the numerically-obtained winding numbers are $n_1 = 1, n_2 = -1$. Thus the resulting lattice is characterized by the topological polarization $\mathbf{P}_T = \mathbf{a}_1 - \mathbf{a}_2$ in terms of the primitive vectors $\mathbf{a}_i$ indicated in Fig. 1c of the main text.

S2. CONSTRUCTING ISOSTATIC NETWORKS WITH DISLOCATIONS

The basic principle for constructing isostatic networks with dislocations was outlined in the main text and Fig. 1. Here we provide more details about the procedure for constructing the lattices used in numerical calculations and the real-world prototypes.

A. Deformed kagome lattice

Following Ref. 1, deformed kagome lattices with non-trivial polarization are obtained by decorating a regular hexagonal lattice with a unit cell consisting of three points and six bonds. The underlying hexagonal lattice is built from the primitive lattice vectors $\mathbf{a}_1 = a\hat{x}$, $\mathbf{a}_2 = (a/2)\hat{x} + (\sqrt{3}a/2)\hat{y}$ where a is the lattice constant and $\hat{x}, \hat{y}$ are unit vectors. Decorating a hexagonal lattice with N points and $3N$ bonds produces a deformed kagome lattice with $3N$ points and $6N$ bonds. We use the parametrization of the unit cell introduced in Ref. 1 to describe deformed kagome lattices with no asymmetry in the constituent triangles: three numbers (x_1, x_2, x_3) quantify the distortion of the lines of bonds away from the straight lines in a regular kagome lattice ($x_i = 0$). Any set of three values x_i specifies the positions of the three points in the unit cell. Equivalently, each bond in the hexagonal lattice is associated with a single point in the kagome lattice. Therefore, for any set of x_i, each bond in a hexagonal lattice can be replaced with a point whose position is calculated from the bond endpoints and the x_i values. Linking up these new points following the bond assignments dictated by the kagome lattice unit cell produces the required deformed kagome lattice as a decoration of the hexagonal lattice.

Numerical lattices with dislocations are prepared starting from a defect-free hexagonal lattice with points connected by harmonic springs of length a and spring constant k under periodic boundary conditions (the system is a rectangular box with dimensions specified to match the size of the finite hexagonal lattice). Using local bond reassignments, a dislocation pair with net zero Burgers vector can be prepared at any location; the individual dislocations can then be moved around independently of each other through a combination of glide and climb steps to obtain the desired separation. The presence of defects necessarily introduces strains in the lattice. Between each glide and climb step, the network of points and springs is relaxed to their (local) minimum energy configuration using a conjugate gradient algorithm. This procedure approximates the elastic strains in a membrane with 2D Young's modulus $2k/\sqrt{3}$ and Poisson ratio $1/3$ [4]. Fig. 1a (main text) shows such an equilibrium configuration around a dislocation in a hexagonal lattice.

Once a relaxed hexagonal lattice with dislocations in the required locations has been created, the decoration described above is carried out. Far away from the defects, the resulting lattice reproduces the relative point positions and bond lengths of the deformed kagome lattice

parametrized by the x_i. However, in the strained regions of the lattice close to the dislocations, the decorated lattice necessarily has triangles that are distorted from their ideal strain-free shape prescribed by the x_i. The dynamical modes of this lattice made out of non-equal triangles can still be numerically calculated (following section S3) under the assumption that every bond is tension-free (i.e. by assigning the bond rest lengths to be exactly equal to the point separations in the decorated lattice), and the resulting spectrum includes approximate zero modes and states of self-stress that follow the count of equation (2), main text. The modes shown in Fig. S3 are calculated using this method, which guarantees that the unit cell matches the expectation from the x_i far away from the defects but at the cost of having irregular triangles near the defect cores.

As mentioned above, elastic distortions of some unit cells are unavoidable when preparing kagome networks from hexagonal lattices with defects under periodic boundary conditions. However, we can reduce the distortions in the triangles making up the kagome network, to bring their shapes closer to the ideal shape in a defect-free lattice and make them visually similar to the physical prototypes which have of triangles of identical shape. We do this *via* the following steps:

1. Decorate the numerically relaxed hexagonal lattice as described above, replacing each bond with a point calculated using the choice of x_i and linking neighbours according to the kagome lattice bond assignment. There is no ambiguity in assigning neighbours to the points near the core of the dislocation, and this assignment satisfies the local constraint count of four neighbours to each site and matches the connectivity of the perfect kagome lattice away from the defect.

2. Assign to each bond in the decorated lattice a rest length that matches the rest length in a defect-free deformed kagome lattice parametrized by x_i. This can be unambiguously done for all bonds in the dislocated kagome lattice except for the edges of a single triangle at the core of each dislocation. For this triangle, we make the following choice: we assign bond lengths to its edges in such a way that the ordered bond length assignment in all six-sided plaquettes surrounding the triangle matches that of six-sided plaquettes in the defect-free lattice.

3. Relax the network of springs to an equilibrium configuration by minimizing the total harmonic spring energy using a conjugate gradient method. Unlike the hexagonal lattice, the kagome lattice has a large space of low-energy deformations that manifest as rotations of the constituent triangles with minimal stretching of the springs, including the soft mode due to the dislocation as well as the long wavelength phonon modes with anomalously low energy described in section S5. These modes dominate the

relaxation of the network, leading to large sections of the lattice with self-intersecting triangles or configurations that deviate significantly from the uniform kagome lattice even far away from the defect. To reduce the influence of the soft modes on the relaxation, we relax the network under a macroscopic strain imposed by increasing the size of the rectangular box, which has the effect of stiffening the network response. For the system shown in Fig. 2a, a strain of 10% along the x direction was imposed during the relaxation step.

4. The kagome lattice after the spring relaxation step has less shape variation among the constituent triangles and six-sided plaquettes when compared to the lattice before the relaxation step. However, the imposition of a macroscopic strain deforms the unit cell away from the original unit cell defined by the x_i. Part of the deformation can be reversed by applying an overall affine deformation to the network that reverses the uniform strain applied in the previous step, returning the periodic box dimensions to their values before the relaxation step. Far away from the dislocations, the network approaches a deformed kagome lattice still built on a hexagonal lattice with primitive vectors $\mathbf{a}_1, \mathbf{a}_2$ unchanged from before, but parametrized by a new set of values $\tilde{x}_i$ that are close to the original x_i.

Upon following the above steps, we obtain a deformed kagome lattice that accommodates the strains required by the dislocations without drastic differences in the shapes of the constituent triangles. The network used for the numerical calculations in Fig. 2a had $(x_1, x_2, x_3) = (0.1, -0.1, -0.1)$ before the relaxation step, which resulted in a deformed kagome lattice parametrized by $(\tilde{x}_1, \tilde{x}_2, \tilde{x}_3) \approx (0.12, -0.06, -0.06)$ away from the dislocation after all steps were followed. The changes in the unit cell due to the relaxation are too small to affect the topological polarization, which depends only on the sign of the x_i [1]. Therefore, we have a reliable procedure to numerically generate deformed kagome lattices, incorporating dislocations under periodic boundary conditions, with a desired topological polarization within the class of lattices introduced in Ref. 1. As Fig. 2a shows, triangles in the network are still distorted by a small amount near the dislocations, because the strains around dislocations in a periodic system cannot be fully accommodated by triangle rotations alone. To calculate the approximate zero modes and states of self-stress, we again redefine the rest lengths of the bonds to match the separations between points in the relaxed configuration so that the network is free of tensions.

Generating deformed kagome networks with dislocations out of near-identical triangles is more straightforward in the physical prototypes. We start with identical laser-cut acrylic triangles with circular holes at the corners. The center-to-center distances of the holes are equal to the bond lengths in a deformed kagome lattice

parametrized by $(x_1, x_2, x_3) = (0.1, -0.1, -0.1)$. We join pairs of triangles at corners with plastic fasteners, which act as hinges. Dislocations can be wired in without difficulty, because of the numerous extra degrees of freedom introduced by the free boundary of the system. These additional degrees of freedom make the structure very floppy, with many unconstrained rotations of triangles about their corner pivots available to accommodate the dislocations. The floppiness is removed from the prototypes by pinning down the boundary points, ultimately producing an overconstrained system. In Fig. 2c, the effect of the dislocations on the network is seen in the (bond length-preserving) distortions of unit cells. The small size of the finite prototype means that the distortions are seen all the way to the boundary, but their amplitude is expected to fall off exponentially over a length scale set by the separation between the dislocations of equal and opposite Burgers vector. A sample many times larger than that constructed could be made to approach a distortion-free kagome lattice at the boundary.

B. Deformed square lattice

Square lattices are another example of isostatic lattices in two dimensions. The regular square lattice, although locally isostatic, does not harbour topologically protected modes since it does not have a gapped phonon spectrum. The presence of straight lines of bonds extending across the lattice gives rise to $2L$ states of self-stress in an $L \times L$ system, and $2L$ corresponding zero modes according to equation (1). These show up as lines of zero modes along $k_x = 0$ and $k_y = 0$ in Fourier space. However, the gap can be opened up everywhere except at $\mathbf{k} = 0$ by decorating the square lattice with a suitable 2×2 unit cell that breaks up the straight lines of bonds. The topologically nontrivial deformed square lattice we use in the main text was obtained by randomly perturbing a regular 2×2 unit cell on a regular square lattice with primitive vectors $\mathbf{a}_1 = a\hat{x}$, $\mathbf{a}_2 = a\hat{y}$. The positions of the four points in the unit cell, defined modulo shifts by Bravais lattice vectors, are $[(0,0), (0.51a, -0.27a), (0.63a, 0.58a), (-0.07a, 0.42a)]$. We have checked numerically that the phonon gap for this particular unit cell closes only at $\mathbf{k} = 0$, which makes $\mathbf{P}_T$ a well-defined quantity. See section S1 for details of the calculation of the polarization vector $\mathbf{P}_T$.

The elementary dislocation in a square lattice (with Burgers vector equal to $\pm \mathbf{a}_i$) can be viewed as a bound pair of two disclinations (defects in lattice orientational order): a lattice point with five-fold symmetry adjacent to a plaquette with three-fold symmetry. The three-fold lattice point disrupts the isostaticity of the Bravais lattice, and also of the resulting crystal lattice after decoration with the 2×2 basis. To prepare dislocations that do not change the local balance between degrees of freedom and constraints, we instead use pairs of disclinations centered on interstitial regions (plaquettes) rather than on

lattice points; an example is shown in Fig. 1c of the main text. Since no lattice point disclinations are used, every lattice point still has exactly four bonds emanating from it. Dislocations constructed in this manner have one of four possible Burgers vectors $\mathbf{b} = \pm(\mathbf{a}_1 \pm \mathbf{a}_2)$, oriented along diagonals of the square plaquettes of the principal lattice. A square lattice incorporating such a dislocation can be decorated with a 2×2 basis to obtain a lattice that maintains isostaticity at each point.

As with the deformed kagome lattices, we numerically create square lattices with dislocation pairs by starting from a defect-free regular lattice, creating a dislocation pair, and separating the pair using glide and climb steps. Between each step we relax the network to its equilibrium structure. To do this, we first fill in the next-nearest-neighbour bonds in the structure so that the network has non-zero bulk and shear moduli. The result is a regular square lattice with elastic strains surrounding the dislocations, as shown in Fig. 1c. Upon decorating this lattice with the 2×2 unit cell while ignoring the strains, we again obtain distorted unit cells close to the defects. We reduce the distortions by following the steps 1–4 outlined for the kagome lattice in the previous section, relaxing the network under external strain after assigning rest lengths to bonds that match the rest lengths in a defect-free lattice with the same 2×2 basis. The unit cell does not define the rest lengths of the bonds traversing the edge shared by the three-fold and the five-fold plaquettes in the base lattice; we arbitrarily reuse rest lengths from the defect-free lattice for these bonds. For the square lattice reported in the main text, we used a macroscopic strain of 5% in both directions during the relaxation step.

S3. NUMERICALLY OBTAINING AND VISUALIZING THE SOFT MODE AND SELF-STRESS

The soft mode plotted in Fig. 2a is obtained by constructing and numerically diagonalizing the dynamical matrix associated with the network. The construction of the network itself follows section S2 A. We start with a hexagonal network of 8,317 nodes in a periodic box of size $128a_0 \times 32\sqrt{3}a_0$ which incorporates two dislocations with Burgers vectors $\pm(\mathbf{a}_1 - \mathbf{a}_2)$, separated by roughly seven lattice constants. We then decorate and relax the lattice to produce a deformed kagome lattice with $(x_1, x_2, x_3) \approx (0.12, -0.06, -0.06)$ in the parametrization of Ref. 1, which has a topological polarization $\mathbf{P}_T = \mathbf{a}_1$. We obtain a network with 24,951 points and twice as many bonds. Figure 2a is a zoomed-in view of a subset of the relaxed network.

The vibrational modes of the structure around this equilibrium are eigenvalues of the dynamical matrix $D = R^\dagger R$, where the rigidity matrix R relates bond extension e_i (one per bond) with node displacement u_j (two per node) via $e_i = R_{ij}u_j$. The rigidity matrix is calculated from the point positions in the equilibrium configuration

(spring constants and node masses are set to 1.) The lowest several eigenvalues (squared frequencies) in order of increasing magnitude and the corresponding eigenvectors of the dynamical matrix are obtained through sparse matrix diagonalization routines implemented in the `Python` programming language. The two lowest eigenvalue modes (with eigenvalues zero up to machine precision) are the trivial translations available to the network under periodic boundary conditions. The first non-trivial eigenvalue (third eigenvalue overall in magnitude) is the proposed topological soft mode associated with the dislocation with dipole moment $\mathbf{d}_A$.

Note that the "collapse mode" identified in periodic locally isostatic networks by Ref. 5 does *not* show up as a zero mode in the numerical spectra of the finite networks. This is because the collapse mode is associated with a change in the shape of the unit cell, and therefore in the shape of the periodic box accommodating a fixed number of unit cells. The numerical calculations are carried out assuming a periodic box of fixed dimensions. Deforming the finite lattice according to a collapse mode would not deform any of the internal bonds of the structure, but it would deform boundary-crossing bonds connecting edge nodes with periodic images of the primary structure. As a result, the collapse mode has a finite energy. If in contrast the periodic box in the simulations were allowed to change its shape, the collapse mode of Ref. 5 would be present in the numerical spectra.

In an infinite system, the topological mode would show up as an eigenvector with eigenvalue zero; in the finite system, it has a finite frequency due to interactions with the other dislocation and with its periodic images. However, it is well-separated in energy from the succeeding modes. The association of the mode with the dislocation on the left is even more apparent in the structure of the corresponding eigenvector, which has its highest amplitude at nodes in a small region of the lattice primarily near the dislocation. In contrast, the eigenvectors of the fourth and higher-frequency modes have the structure of periodic acoustic modes that extend over the entire lattice.

The eigenvector corresponding to each eigenvalue gives a displacement (a two-dimensional vector) at each point; the magnitude of each displacement vector corresponds to the relative amplitude of the mode at that point. (The absolute magnitude of the displacements has no physical significance.) In figures 2a–b, we have plotted these displacements for the eigenvector corresponding to the third eigenvalue as red arrows, each indicating the direction and scaled in size by the relative magnitude of the displacement of the point at its base. (Red dots replace arrows whose length is less than the dot diameter.)

Whereas the eigenvectors of the dynamical matrix correspond to normal modes, the eigenvectors of its "super-symmetric partner" $\tilde{D} = RR^\dagger$ [1] correspond to tensions and compressions experienced by the individual bonds when the system is driven with the normal modes. Each component of the eigenvector translates to a tension on a particular bond. States of self-stress are eigenvectors of the partner matrix with eigenvalue zero; the eigenvector corresponding to the smallest eigenvalue of the partner matrix is localized (i.e. has appreciable tension values) to bonds in the vicinity of the dislocation with dipole moment $\mathbf{d}_B$. This eigenvector is visualized in figure 2b by increasing the width of each bond (linearly over the range w to $4.6w$, where w is the width of the thinnest bond in the figure) by an amount proportional to the magnitude of the tension. The colour on each bond is also set by the tension; it interpolates between blue (negative tensions) and magenta (positive tensions) with gray bonds signifying low or no tension.

The calculation and visualization of modes of the deformed square lattice in Fig. 2b follows a similar procedure. We follow the steps outlined in section S2 B, starting with a square lattice of 24,766 nodes in a periodic box of dimensions $192a_0 \times 128a_0$, and decorate and relax the lattice to get a deformed square lattice of 99,064 points, a small region of which is displayed in Fig. 2b with the soft mode and approximate state of self-stress visualized as described above.

An interesting distinction between the two networks we study numerically in the main text is that the mode count associated with the left dislocation, as predicted by equation (2), is $+1$ in the deformed kagome lattice and $+2$ in the deformed square lattice. Fig. S1 verifies the mode count for the square lattice by showing the two lowest eigenmodes of the dynamical matrix for the network used in Fig. 2b, but with *pinned* boundary conditions. The pinning reduces the interactions between the localized modes and the long-wavelength modes of the system and eliminates the wraparound nature of the long "tail" of the mode in the slow localization direction. This enhances the distinction between the modes localized to the left dislocation and the other low-energy modes, which are not localized to either dislocation. This figure also shows that pinning the boundary, which creates an overconstrained system which is no longer strictly isostatic, does not eliminate the topological soft modes. This fact is also verified by the physical prototype based on the deformed kagome lattice.

S4. ZERO MODE COUNT OF A LATTICE CONTAINING A DISLOCATION

Kane and Lubensky [1] proved that the number of zero modes minus the number of states of self-stress in a lattice subsystem S, ν^S, decomposes into a sum

$$\nu^S = \nu_L^S + \nu_T^S, \tag{S3}$$

where ν_L^S is a "local" count and ν_T^S is a "topological" count. The local count ν_L^S is related to the number of unit cells of the system included in S. If the unit cell is chosen so that the term $\mathbf{r}_0$ is zero, then by choosing the subsystem S appropriately, ν_L^S can be arranged to be zero.
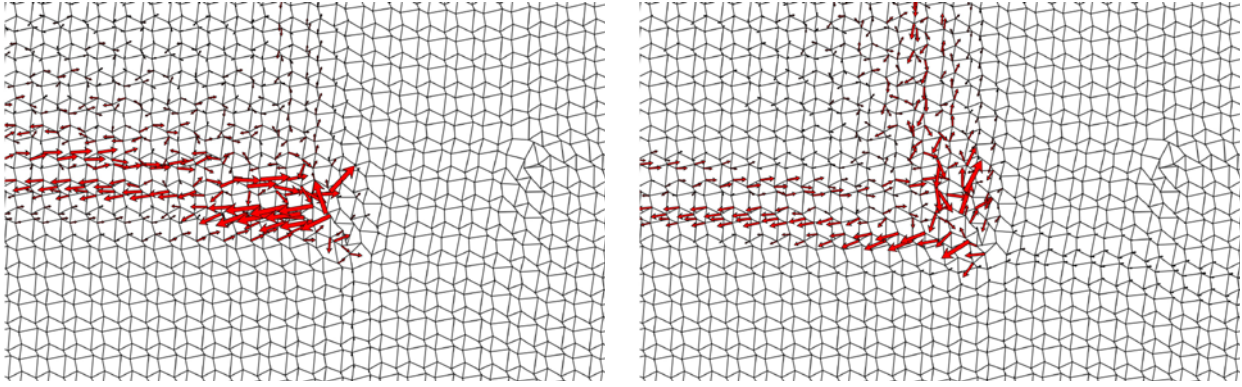
FIG. S1. Visualization of the eigenvectors of the dynamical matrix of the network in Fig. 2b with the lowest (left) and next-lowest (right) eigenvalues, when the dynamical matrix is evaluated under pinned boundary conditions. Pinning the boundary is implemented by eliminating the degrees of freedom associated with points within $2a$ of the boundary, yielding a rigidity matrix with fewer columns. Such a setup replicates the pinned boundary conditions used in the physical prototypes, and results in a system that is overconstrained, yet exhibits soft modes associated with dislocations of the correct orientation.

If S is bounded by the contour $\mathcal{C}$, Kane and Lubensky [1] showed that ν_{T}^S is given by the formula

$$\nu_{\mathrm{T}}^S = \oint_{\mathcal{C}} \frac{d^{d-1}S}{V_{\mathrm{cell}}} \mathbf{P}_{\mathrm{T}} \cdot \hat{n}, \qquad (S4)$$

where $\hat{n}$ is the inward-pointing normal to the boundary, and V_{cell} is the d-dimensional volume of the unit cell.

To compute the zero mode count associated with a dislocation, we need to evaluate the integral in Eq. S4 for a path surrounding a single dislocation in a lattice with topological polarization $\mathbf{P}_{\mathrm{T}}$ (as defined in section S1). We consider paths where $\nu_L^S = 0$ to focus on the effects of the dislocation.

We compute this integral by taking into a account the deformations in the lattice due to the dislocation, in the continuum limit. The dislocation induces a displacement field $\mathbf{u}$ around it. We can choose a path sufficiently far away from the dislocation core so that the resulting lattice distortions do not change the topological winding numbers n_i from their values in the undistorted lattice. Then, any variation in $\mathbf{P}_{\mathrm{T}} = \sum_i n_i \mathbf{a}_i$ comes only from changes in the local lattice vectors $\mathbf{a}_i$. In the continuum limit ($\mathbf{a}$ smaller than the scale of variation of $\mathbf{u}$), these are determined by the displacement fields, and as a result we have a position-dependent polarization

$$P_{\mathrm{T}i} = P_{\mathrm{T}i}^0 + w_{ji}(\mathbf{x}) P_{\mathrm{T}j}^0, \qquad (S5)$$

where

$$w_{ji}(\mathbf{x}) = \partial u_i / \partial x_j \qquad (S6)$$

is the distortion tensor and $\mathbf{P}_{\mathrm{T}}^0$ is the polarization in the undistorted lattice. Meanwhile, the volume of the distorted unit cell is

$$V_{\mathrm{cell}}(\mathbf{x}) = V_{\mathrm{cell}}^0 (1 + w_{ii}) \qquad (S7)$$

to linear order in the displacements. Writing out Eq. S4 to linear order in w_{ij}, we have

$$\nu_{\mathrm{T}}^S = \oint_{\partial S} \frac{dS}{V_{\mathrm{cell}}^0} \hat{n}_i \left[P_{\mathrm{T}i}^0 + w_{ji} P_{\mathrm{T}j}^0 - w_{jj} P_{\mathrm{T}i}^0 \right] \qquad (S8)$$

$$= -\frac{1}{V_{\mathrm{cell}}^0} \int_S dA\, \partial_i \left[P_{\mathrm{T}i}^0 + w_{ji} P_{\mathrm{T}j}^0 - w_{jj} P_{\mathrm{T}i}^0 \right] \qquad (S9)$$

$$= \frac{1}{V_{\mathrm{cell}}^0} \int_S dA\, P_{\mathrm{T}i}^0 \left[\partial_i w_{jj} - \partial_j w_{ij} \right], \qquad (S10)$$

where we use the divergence theorem to convert the line integral to an area integral (note that $\hat{n}$ is the *inward* pointing normal to the contour). However, the distortion tensor is related to the Burgers vector via [6]

$$b_k = -\int_S dA\, \varepsilon_{ij} \partial_i w_{jk}. \qquad (S11)$$

Upon applying the antisymmetric tensor to both sides, we get

$$\varepsilon_{km} b_k = -\int_S dA\, \varepsilon_{ij} \varepsilon_{km} \partial_i w_{jk} \qquad (S12)$$

$$= \int_S dA\, (\delta_{im} \delta_{jk} - \delta_{ik} \delta_{mj}) \partial_i w_{jk} \qquad (S13)$$

$$= \int_S dA\, (\partial_m w_{kk} - \partial_k w_{mk}). \qquad (S14)$$

The vector on the left-hand side, obtained by rotating the Burgers vector by $\pi/2$ counterclockwise, is the dipole moment associated with the pair of disclinations that make up the dislocation, which we call $\mathbf{d}$. For an elementary dislocation in the hexagonal lattice, this is a vector of length a_0 that points from the fivefold to the sevenfold point. Equations S10 and S14 together give the topological count in terms of the disclination dipole moment,

$$\nu_{\mathrm{T}}^S = \frac{1}{V_{\mathrm{cell}}^0} P_{\mathrm{T}i}^0 \varepsilon_{ji} b_j = \frac{1}{V_{\mathrm{cell}}^0} \mathbf{P}_{\mathrm{T}} \cdot \mathbf{d}. \qquad (S15)$$

S5. LOCALIZATION PROPERTIES OF TOPOLOGICALLY PROTECTED MODES

The numerical results of the main text show that, in certain spatial directions away from the dislocation, the decay of the amplitude of the soft mode associated with a dislocation is much slower than in the other directions (Fig. 3, main text). We observe here that these directions appear to be controlled by the long-wavelength elastic behaviour of the bulk lattice without defects.

The authors of Ref. 1 showed that in the long-wavelength limit of the elasticity of the deformed kagome structures with $\mathbf{P}_{\mathrm{T}} \neq 0$, there are two directions in the Brillouin zone which exhibit anomalous dispersion of the long-wavelength acoustic modes as a function of the wavevector $\mathbf{k} = (k_x, k_y)$. Along these directions, the bulk modes have a dispersion that scales as $\omega \sim k^2$ rather than the typical situation for acoustic phonon modes which is $\omega \sim k$. These directions are revealed by expanding the determinant of the Fourier-transformed rigidity matrix $R(\mathbf{k})$ in powers of (k_x, k_y); along the special directions, characterized by $k_x = \alpha_i k_y$ ($i \in \{1, 2\}$) where α_1 and α_2 are determined by the unit cell, $\det R$ vanishes to quadratic order in k [1]. Therefore, $k_x = \alpha_i k_y$ specify lines of modes that are gapless to quadratic order in k, whose energy is made finite only by the presence of higher-order terms. Such near-gapless lines in the dispersion indicate a multitude of low-energy modes of the lattice whose associated displacements are constant along the special directions $y = \alpha_i x$ in real space.

We observe that the directions of weak localization of the topological soft modes in real space tracks these special directions originating in the anomalous dispersion in $\mathbf{k}$-space. Fig. S2 compares the directions of weak localization of the topological modes (dashed lines) to the directions of anomalous dispersion in $\mathbf{k}$-space (sharp lines in density plot). As mentioned earlier, the deformed kagome lattice used for the lattices and prototypes studied in the main text corresponds to $(x_1, x_2, x_3) = (.12, -.06, -.06)$ in the parametrization of Ref. 1. For such a lattice, $\alpha_1 = -\alpha_2$ [1] (we obtain specifically $\alpha_i = \pm\sqrt{(3x_1)/(x_1 - 4x_2)} \approx \pm 1$). We numerically obtain a similar feature in the determinant of the Fourier-transformed rigidity matrix of the deformed square lattice, with the two directions $k_x = \alpha_i k_y$ along which $\det R = 0$ to quadratic order in k quantified by $\alpha_1 \approx 9.995$ and $\alpha_2 \approx 0.105$. In both lattices, the directions of weak localization are consistent with the real-space directions of soft response corresponding to the near-gapless lines, $y = \alpha_i x$ (the special directions in real space and $\mathbf{k}$-space are related by a $\pi/2$ rotation, thus the axes of the Brillouin zone in Fig. S2 have been swapped to make the correspondence more apparent).

This behaviour is confirmed numerically in other members of the class of deformed kagome lattices of Ref. 1, parametrized by $(x_1, x_2, x_3) = (x_1, -0.1, -0.1)$, for which $\alpha_1 = -\alpha_2 = \sqrt{(3x_1)/(x_1 - 4x_2)}$. Upon increasing x_1 from zero, the weak localization direction in real space tracks the change in anomalous dispersion direction in $\mathbf{k}$-space, as illustrated in Fig. S3, again suggesting that the origin of the former lies in the latter. Establishing the theoretical relation between the two special directions would be an interesting avenue for future work.

[1] C. L. Kane and T. C. Lubensky, Nature Physics **10**, 39 (2014).

[2] J. E. Graver, B. Servatius, and H. Servatius, *Combinatorial rigidity*, Vol. 2 (American Mathematical Soc., 1993).

[3] C. Calladine, International Journal of Solids and Structures **14**, 161 (1978).

[4] H. Seung and D. Nelson, Physical Review A **38**, 1005 (1988).

[5] V. Kapko, M. M. Treacy, M. F. Thorpe, and S. Guest, Proceedings of the Royal Society A: Mathematical, Physical and Engineering Science **465**, 3517 (2009).

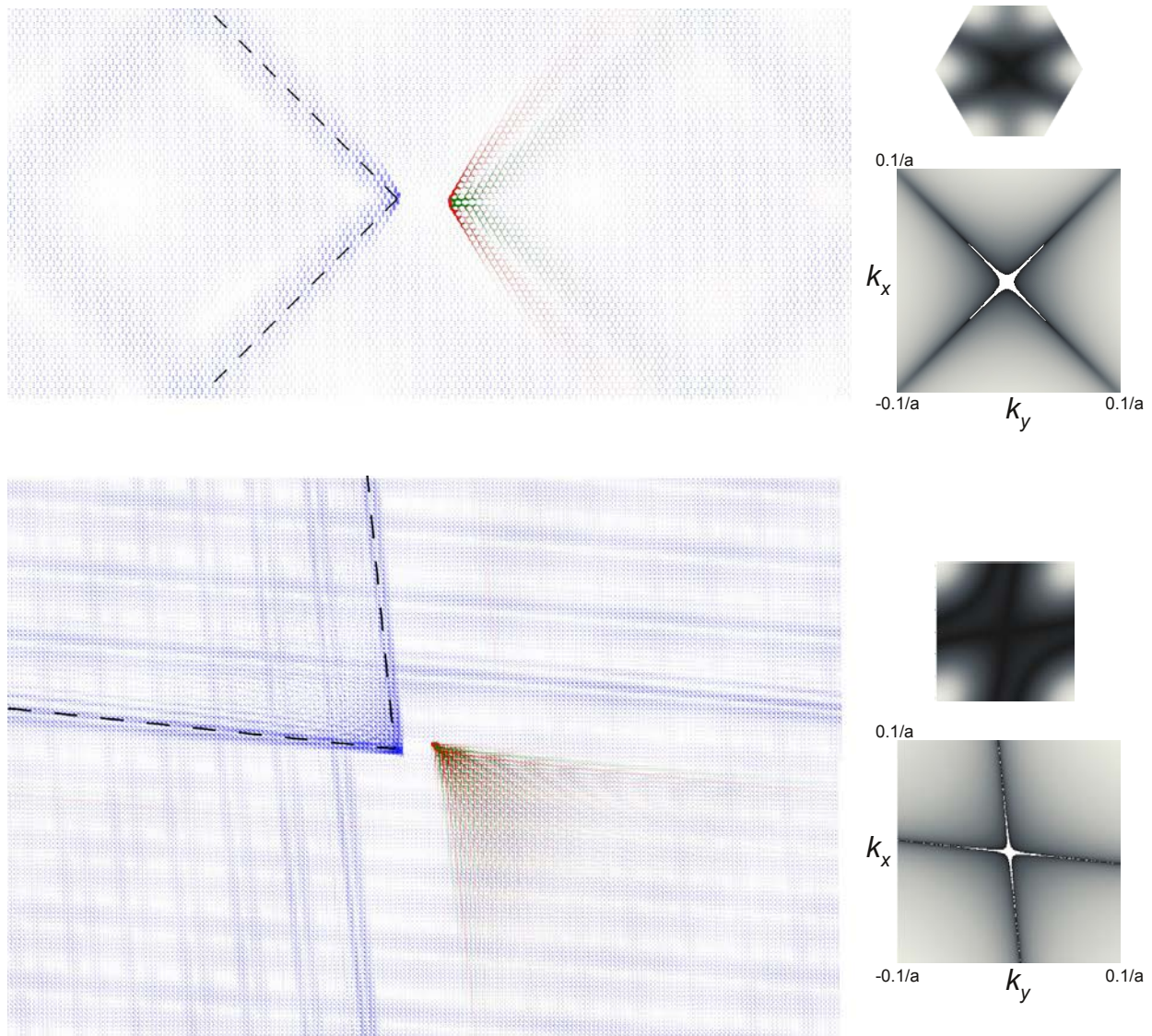[6] L. D. Landau and E. M. Lifshitz, *Theory of Elasticity*, 3rd ed. (Butterworth Heinemann (Oxford)).

FIG. S2. Zoomed-out versions of the scatter plots of the mode amplitude from Fig. 3 of the main text. The entire lattice is shown for both the kagome- and square-based topological lattices (consisting of 128×64 unit cells for the deformed kagome and 192×128 unit cells for the deformed square lattice). The approximate state of self-stress associated with the opposite dislocation is also visualized for each lattice by scaling the thickness of bonds by the magnitude of the tension (green) or compression (red) as in main text Fig. 2. The wrapping of the weak localization direction around the periodic boundaries is apparent. To the top right of each lattice is a density plot of $\det R$ as a function of $\mathbf{k}$ in the respective Brillouin zone. Below this, a density plot of $\log \det R$ is shown for a subsection of the Brillouin zone near the origin, to highlight the directions of anomalous dispersion (sharp lines) along which $\det R = 0$ to quadratic order in (k_x, k_y). The axes of the Brillouin zone have been swapped to aid the visual comparison of the localization direction in real space and the anomalous dispersion directions in momentum space.

$(x_1, x_2, x_3) = (0.02, -0.10, -0.10)$

$(x_1, x_2, x_3) = (0.05, -0.10, -0.10)$

$(x_1, x_2, x_3) = (0.10, -0.10, -0.10)$
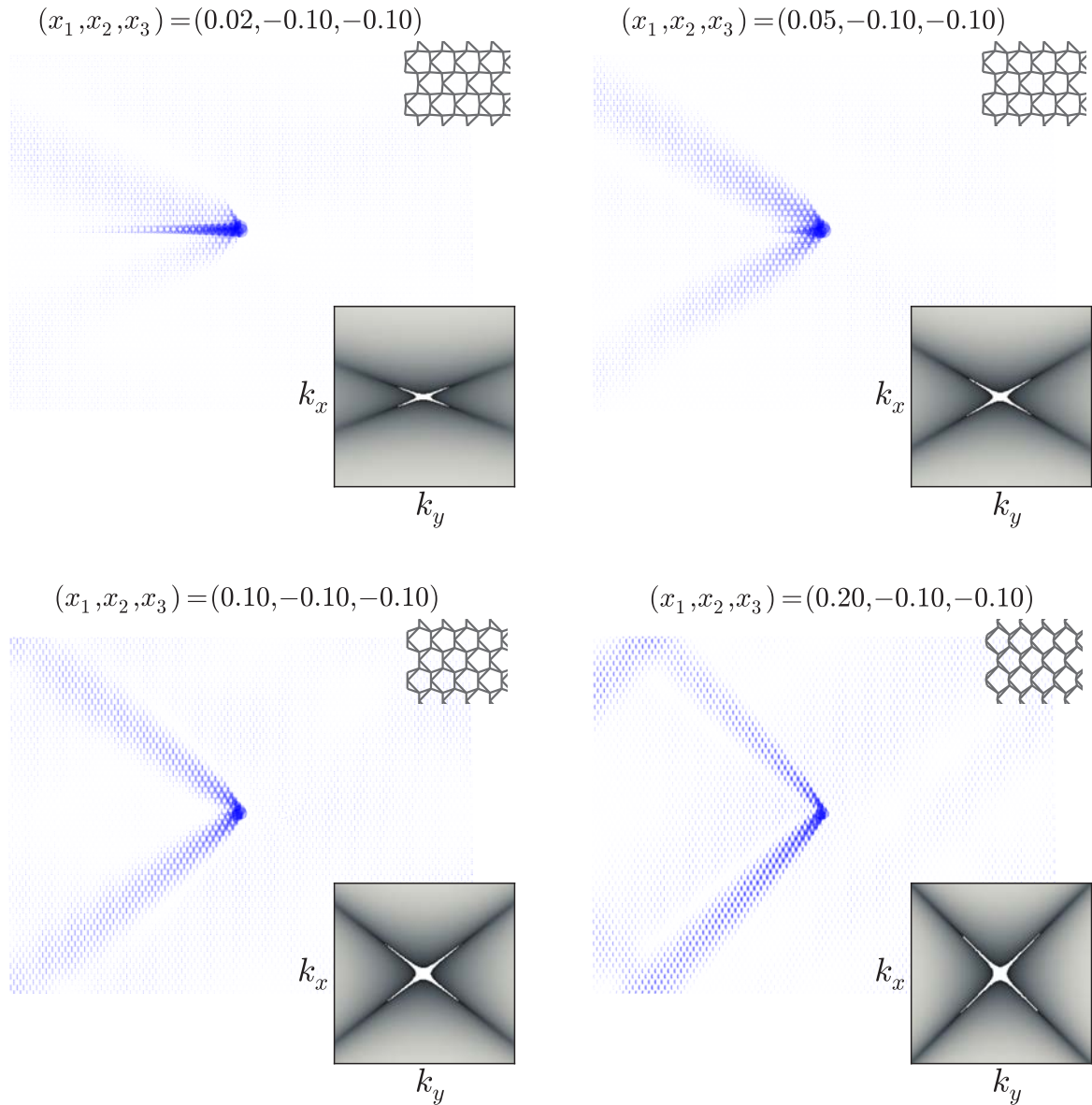
$(x_1, x_2, x_3) = (0.20, -0.10, -0.10)$

FIG. S3. Scatter plots similar to Fig. S2 for the numerically-obtained soft mode associated with a dislocation in four different deformed kagome lattice unit cells parametrized by $(x_1, x_2, x_3) = (x_1, -0.1, -0.1)$. The lattices are 128×64 unit cells in size, and have a dislocation and anti-dislocation with the same orientations and separation as in Fig. 3a of the main text. A section of the defect-free lattice is shown in the upper right corner of each scatter plot to illustrate the unit cell, and a density plot of $\log \det R$ near the origin of the Brillouin zone is shown in the lower right corner to indicate the directions of anomalous dispersion. The density plot is rendered with k_x on the vertical axis to highlight the visual similarity with the directions of weak localization of the soft mode in real space.